Research in Astronomy and Astrophysics, 23:015020 (12pp), 2023 January https://doi.org/10.1088/1674-4527/aca7df

Micro-vibration Modeling and Verification of Shutter Mechanism of Survey Space Telescope

Tong-Lei Jiang[1,2], Li-Hua Wen[1], Hu Zhan[2], Bo Wang[1], and Yong-Chao Yang[1]

[1] School of Astronautics, Northwestern Polytechnical University, Xi'an 710072, China; tonglei87@mail.nwpu.edu.cn

[2] National Astronomical Observatories, Chinese Academy of Sciences, Beijing 100101, China

Received 2022 August 23; revised 2022 November 10; accepted 2022 November 23; published 2023 January 11

Abstract

The scientific research mission of the Survey Space Telescope (also known as the China Space Station Telescope, CSST) imposes rigorous requirements on the observation precision. However, microvibrations generated by the shutter mechanism can seriously affect the performance of the highly precise and sensitive instruments onboard. This study presents a dynamic model and verifies its performance using experimental results. Indeed, a five-degree-of-freedom nonlinear dynamic model that considers all interference sources and bearing nonlinearity is established. The validity of the proposed model is verified using experimental measurements of the microvibration characteristics. The obtained results proved that the proposed dynamic model can accurately predict the characteristics of the microvibrations caused by the shutter mechanism in the design stage and provide a theoretical basis for the development of CSST.

Key words: telescopes – surveys – methods: numerical – methods: analytical

1. Introduction

The Survey Space Telescope (also known as the China Space Station Telescope, CSST) expected to be operational approximately in 2024. In addition, it will be primarily used for large-scale multi-color imaging and slitless spectroscopy surveys in addition to thorough studies on selected astronomical objects or regions using a variety of observational techniques (Su & Cui 2014; Gao et al. 2015). CSST is equipped with five instruments, of which the survey module is the most key scientific payload. Indeed, CSST can scientifically observe astronomical regions of approximately 17,500 square degrees at an angular resolution close to that of the Hubble Space Telescope (HST) (Zhan 2011). This imposes rigorous requirements on the performance of the telescope and accuracy of data processing. Thus, the static errors in the central 1.1 square degree field-of-view and 80% energy concentration point-spread function (PSF) radius R_{EE80} for the attitude control, image stabilization, microvibrations, and other dynamic factors should not be greater than $0\farcs15$ and the PSF ellipticity should not be greater than 0.15 (Zhan 2021). Thus, microvibrations caused by individual systems during the operation of CSST must be explored. Micro-vibrations are reciprocating motions or oscillations with a small amplitude on the spacecraft structure caused by the normal operation of the internal moving components of the spacecraft and mechanical effects of the external environment during the spacecraft operation in orbit. Analysis of the microvibrations is crucial for the study of large space telescopes (Li et al. 2018). After its launch, the reaction wheel of HST has been producing unintended microvibrations, seriously affecting the pointing accuracy and preventing an appropriate operation. Therefore, microvibrations have gradually garnered considerable attention and many studies have been conducted on microvibrations (Davis et al. 1986). For example, microvibrations have been thoroughly studied in the theoretical development stage of the James Webb Space Telescope (JWST) and Eclipse Telescopes with high-pointing accuracy and stability requirements (Meza et al. 2005). Many critical tasks must be accomplished to accurately determine the characteristics of microvibrations. Thus, an accurate dynamic model is needed for predicting microvibration disturbance. In addition, accurate disturbance data from vibration sources should be collected to investigate the characteristics of microvibrations (Tang et al. 2020). The main sources of microvibrations in space optical telescopes include the inertial gyroscopes, momentum wheels, cry coolers, and camera shutters (Liu et al. 2015). The development of the previously launched HST and JWST has proved that obtaining accurate disturbance data in the early stages of construction is significant. The accuracy of the obtained characteristics of microvibrations depends on the accuracy of the derivation method and that of the model. Most studies on the characterization of microvibrations have considered microvibrations caused by the momentum wheels and coolers, whereas microvibrations caused by shutters have been scarcely investigated. Dynamic characteristics of the shutter mechanism are comparable to those of the rotor-bearing system of a flywheel. Hence, the models developed to study rotor-bearing systems are highly beneficial for analyzing the shutter mechanism.

Many models have been developed to explore the generation of microvibrations in rotating-like operation modes. Hasha (1986) proposed an empirical model to analyze the disturbances of the HST flywheel system. The model considered the microvibration disturbance as a series of forces with different amplitudes and frequencies. In addition, the reaction wheel was tested under different conditions and analyzed by comparing the experimental results. However, this method is typically used in the later stages of product testing, and cannot provide a scientific guidance to study the characteristics of microvibrations in the theoretical development stage. Liu et al. (2008) combined theoretical and experimental modeling to propose a model based on the rotor dynamics. The model was established theoretically, and empirical modeling was used where theoretical modeling was difficult. Liu et al. (2008) used both the resonant and broadband disturbances as the input for the derivation and modeling of the structural dynamics. Subsequently, disturbance tests were performed on the system, and the experimental data were used to correct the analytical model and finalize the disturbance model. As for dynamic models for rotating-type microvibrations, Masterson et al. (2002) proposed a dynamic model for a flywheel. The unbalanced mass of a flywheel was theoretically modeled followed by considering other disturbance sources through experimental methods. This method regarded all factors associated with the microvibrations, and the model could be readily established. However, the model cannot provide accurate microvibration data at the theoretical design stage, and subsequent tests are necessary to predict microvibration levels satisfactorily. Alkomy & Shan (2021) and Zhou et al. (2012) developed a theoretical model considering the nonlinear stiffness for the microvibrations generated by a flywheel with an unbalanced mass. However, the fully theoretical model needs to consider both linear and nonlinear problems, increasing the complexity of the model development and computation time. Nevertheless, the model can provide an accurate guidance for product design in the theoretical design stage, thus microvibrations can be accurately or with minor modifications characterized in the first production. However, the complexity of the method has limited the studies on this subject. The mass imbalance of the rotor is typically considered as the primary source of disturbance, where its disturbance frequency and frequency of rotation are equal. When the frequency of rotation overlaps with the natural frequency, resonance occurs and the disturbance is infinitely amplified (Wang et al. 2017; Xia et al. 2021). Unlike the modeling of rotating systems, such as flywheels, the shutter component has a low rotation speed and large eccentric mass, thus the effect of the flexible deformation of their blades on the disturbance force should be considered. Although microvibrations caused by reaction flywheels have been extensively studied, the effect of microvibrations generated by camera

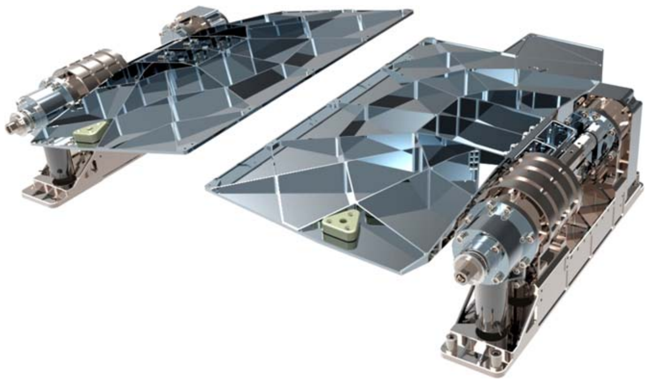

Figure 1. Structure of shutter of CSST.

shutters have been insufficiently explored. Liang (2021) established a mathematical model for the microvibrations generated by a bi-parting mechanical shutter using a mathematical model for a rigid rotating rotor. The excitation force of the rotating bi-parting shutter exhibited low-frequency microvibrations, which were canceled in the direction of the rotating bi-parting and doubled in the direction normal to the plane of the two axes. With the increasing usage of the shutter component in large space telescopes, the characteristics of the associated microvibrations must be urgently investigated. The derivation of an accurate dynamic model of the shutter is critical because it significantly affects both the design and manufacturing processes. In this study, a theoretical and analytical dynamic model of the shutter is proposed. The disturbance forces generated during the blade rotation and nonlinear stiffness of the bearing are modeled using the Hertzian contact theory. To validate the performance of the proposed model, the simulation and experimental results are compared.

The remainder of this paper is organized as follows. In Section 2, the analytical derivation of the dynamic model, including the disturbance sources, is presented. The simulation and experimental results are presented in Sections 3 and 4, respectively. Section 5 discusses and analyzes the results. Finally, Section 6 draws the conclusions.

2. Theoretical Dynamic Model

The shutter is located at the front of the focal plane. Indeed, it is mounted on the main structure of the survey camera with the focal plane. The bi-parting mechanical shutter mechanism comprises two groups of single side shutters and two groups of shutter blades that rotate in reverse synchronously to accomplish the opening or closing of the shutter. During the shutter rotation, the shutter shaft undergoes deflection and generates microvibrations owing to the rotational force of the blade. In this study, a dynamic model for a single side shutter is presented, the structure of the single side shutter is shown in

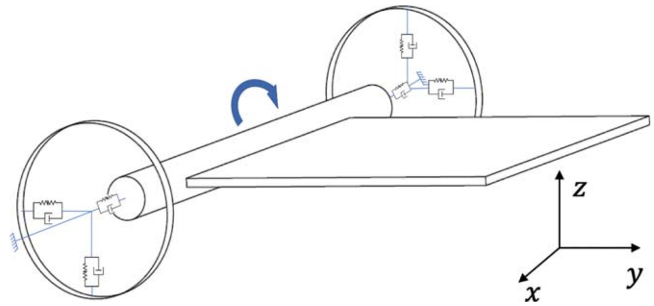

Figure 2. Simplified model of the shutter structure.

Figure 1. The single side shutter is mainly supported by angular contact bearings, which can be simplified into a support structure, as shown in Figure 2. As the rotation speed of the blade is low and stiffness of the shutter rotation shaft is large, its natural frequency is considerably higher than that of other components. Hence the rotation shaft can be assumed as a rigid body.

2.1. Dynamic Model of the Micro-vibrations from the Shutter

The dynamic model of the shutter was established using the energy method. In this study, the following coordinate systems are defined: the overall spacecraft coordinate system is the spatial inertial coordinate system xyz, where the coordinate system of the bearing-rotation shaft system is $x_k y_k z_k$. Six degrees of freedom in the deflection of the shutter rotation shaft include two degrees of freedom along the radial direction (u, v), one degree of freedom in the axial direction (ω), and deflection in three directions of α, β, γ. The relationship between the shutter coordinate system $x_k y_k z_k$ and spatial inertial coordinate system xyz after the shutter undergoes deflection is depicted in Figure 3. In this case, the shutter shaft rotates at a constant speed of $\dot{\alpha}$, and dynamics in the direction of the shutter rotation is ignored.

The conversion matrix after deflection is calculated according to the Euler angular conversion as

$$T^K = \mathrm{Rot}(\beta)\mathrm{Rot}(\gamma), \tag{1}$$

where

$$[\mathrm{Rot}(\beta) = \begin{bmatrix} \cos\beta & 0 & -\sin\beta \\ 0 & 1 & 0 \\ \sin\beta & 0 & \cos\beta \end{bmatrix},$$
$$\mathrm{Rot}(\gamma) = \begin{bmatrix} \cos\gamma & -\sin\gamma & 0 \\ \sin\gamma & \cos\gamma & 0 \\ 0 & 0 & 1 \end{bmatrix}. \tag{2}$$

In this study, the dynamic model of the shutter was established using the Lagrangian function, whose general form

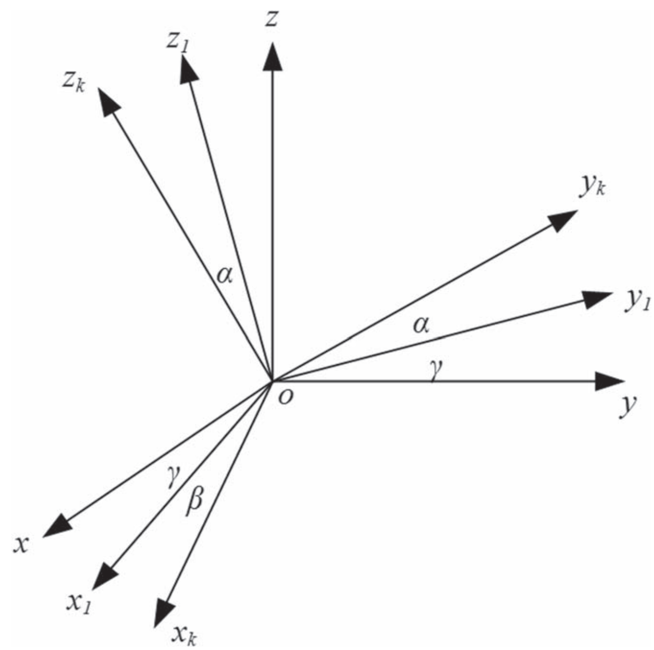

Figure 3. Eulerian transformation relationship of the coordinate systems.

is expressed as follows:

$$\frac{d}{dt}\left(\frac{\partial T}{\partial \dot{q}}\right) - \frac{\partial T}{\partial q_i} + \frac{\partial V}{\partial q_i} + \frac{\partial D}{\partial \dot{q}_i} = Q_i,$$
$$i = 1, 2, 3, \cdots, n, \tag{3}$$

where q is the generalized coordinate, Q_i is the nonother potential generalized force beyond the corresponding potential, and D is the energy dissipation function, which is defined as the work completed by the damping of the system during vibrations.

The generalized degrees-of-freedom of the shutter rotation shaft is expressed as

$$q_k = [q_{k1}^T \; q_{k2}^T]^T = [u \; v \; w \; \beta\gamma]. \tag{4}$$

According to Equation (3), the translation and deflection speeds of the shutter rotation shaft can be expressed respectively as

$$\nu_k|_{x_k y_k z_k} = [\dot{u}\dot{v}\dot{w}]^T, \tag{5}$$

where

$$[\dot{\omega}_k|_{x_k y_k z_k} = \begin{bmatrix} 0 & 0 & -\sin\beta \\ 0 & 1 & 0 \\ 0 & 0 & \cos\beta \end{bmatrix} \begin{bmatrix} \dot{\alpha} \\ \dot{\beta} \\ \dot{\gamma} \end{bmatrix}$$
$$+ \begin{bmatrix} \dot{\alpha} \\ 0 \\ 0 \end{bmatrix} = \begin{bmatrix} 1 & 0 & -\sin\beta \\ 0 & 1 & 0 \\ 0 & 0 & \cos\beta \end{bmatrix} \begin{bmatrix} \dot{\alpha} \\ \dot{\beta} \\ \dot{\gamma} \end{bmatrix}. \tag{6}$$

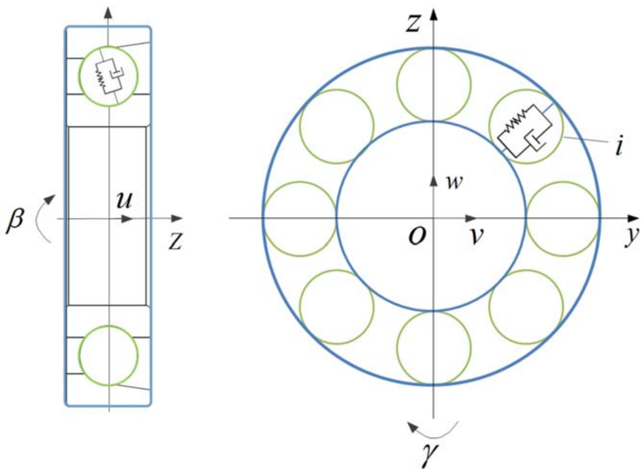

Figure 4. Bearing structure and its simplified model.

The kinetic energy of the shutter rotation shaft system is

$$T_k = \frac{1}{2} v_k^T m_k v_k + \frac{1}{2} \omega_k^T I_k \omega_k, \tag{7}$$

where M_k and I_k are the mass and inertia distribution matrices of the shutter rotation shaft.

$$m_k = dia\, g[m_k\ m_k\ m_k],\ I_k = dia\, g[I_r\ I_r]. \tag{8}$$

The elastic potential energy of the system can be expressed as

$$V_k = \frac{1}{2} q_{k1}^T k_t q_{k1} + \frac{1}{2} q_{k2}^T k_r q_{k2}, \tag{9}$$

where k_t and k_r are the translational stiffness and rocking stiffness matrices of the shutter rotation shaft.

The energy consumed by the system damping is expressed as

$$D_k = \frac{1}{2} v_k^T c_t v_k + \frac{1}{2} \omega_k^T c_r \omega_k, \tag{10}$$

where c_t and c_r are the translational damping and rocking damping matrices of the shutter rotation shaft.

2.2. Dynamic Modeling of the Bearing

An angular contact bearing is used to connect the shutter central rotation shaft and support stand. When the bearing rotates, an elastic effect among the ball units appears. During the rotation process, the ball-track contact pair undergoes an elastic vibration under the excitation conditions (Liu et al. 2019). Therefore, nonlinear stiffness characteristics of the bearing need to be considered. Figure 4 shows the equivalent analysis model of the bearing vibration. The ball-track contact pair is equivalent to a spring-damper oscillator, which is modeled using the Hertz theory (Hernot et al. 2000).

According to the elastic contact relationship in the Hertzian contact theory, the elastic contact force f_i between the i-th ball unit and track can be expressed as

$$f_i = k_i (\Delta d_i)^{\frac{3}{2}}, \tag{11}$$

where Δd_i is the deformation of the ball at the contact point along the normal direction, and k_i is the elastic stiffness coefficient of the contact. In addition, k_i can be calculated as follows

$$k_i = \left[\left(\frac{1}{k_{ii}} \right)^{2/3} + \left(\frac{1}{k_{io}} \right)^{2/3} \right]^{-3/2}, \tag{12}$$

where k_{ii} and k_{io} denote the elastic coefficients between the ball and the inner and outer tracks, respectively, which can be calculated using the Young's modulus and Poisson's ratio of the ball material and the curvature at the contact point.

When the changed amplitude of load Δf_i is not large compared to the average load f_0, the stiffness of the ball-raceway contact pair can be approximated as

$$k_{i1} = \frac{df_i}{d\Delta d_i} |_{f_i = f_{\text{pre}-i}} = \frac{3}{2} (k_i^2 f_{\text{pre}-i})^{\frac{1}{3}}, \tag{13}$$

where $f_{\text{pre}-i}$ is the load in the direction normal to the contact pair for a single ball under the preload f_{pre}.

$$f_{\text{pre}-i} = \frac{f_{\text{pre}}}{NZ \sin \alpha_k}, \tag{14}$$

where N is the number of bearings, Z is the number of balls in a single bearing, and α_k is the contact angle between the balls and track. In addition, Δd_i can be approximated by the rigid body motion of the bearing as (Luo et al. 2013).

$$\Delta d_i \approx N_i q_k. \tag{15}$$

At the position of the steel ball i, let the axial and radial displacements of the bearing be u_{ia} and u_{ir} , respectively. Then (Hernot et al. 2000)

$$u_{ia} = u_x + r\theta_z \sin \varpi_i - r\theta_y \cos \varpi_i, \tag{16}$$

$$u_{ir} = u_z \cos \varpi_i + u_y \sin \varpi_i. \tag{17}$$

The total variation of the i-th steel ball along the contact normal i is expressed as

$$\Delta d_i = u_{ir} \cos \alpha_k + u_{ia} \sin \alpha_k, \tag{18}$$

where

$$N_i = \begin{Bmatrix} \sin \alpha_k \\ \sin \varpi_i \cos \alpha_k \\ \cos \varpi_i \cos \alpha_k \\ -r \cos \varpi_i \sin \alpha_k \\ r \sin \varpi_i \sin \alpha_k \end{Bmatrix}, \tag{19}$$

where ϖ_i is the angular position of the i-th ball in the track. The speed $\dot{\alpha}$ of the inner track of the bearing and rotation axis are

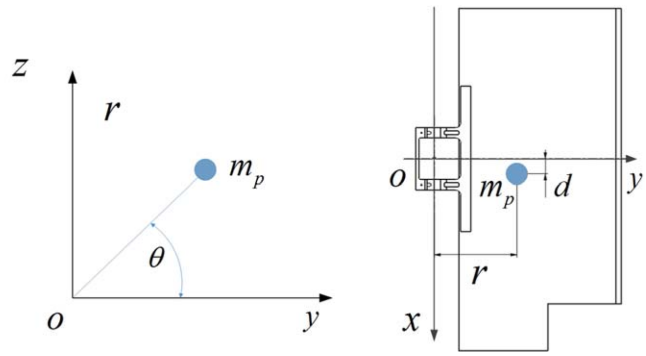

Figure 5. Static and dynamic imbalances modeling.

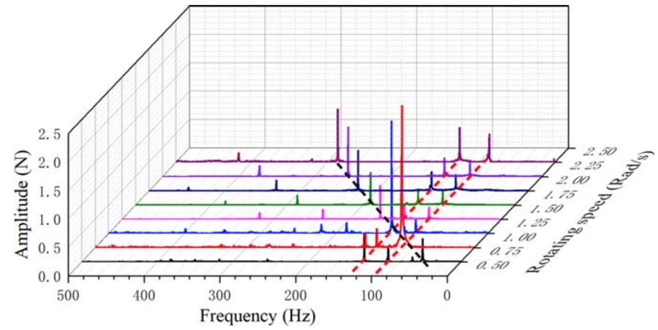

Figure 6. Simulation results of disturbance forces in X-direction.

identical. Subsequently, ϖ_i can be expressed as

$$\varpi_i = 0.5(1 + D_{kb}D_{km}^{-1}\cos\alpha_k) \times \dot{\alpha}t + \frac{2\pi(i-1)}{Z}, \tag{20}$$

where D_{km} and D_{kb} are the diameters of the bearing pitch circle and ball, respectively.

According to Equations (11)–(20), the V_k by the bearing system can be expressed as

$$V_k = -q_k^T \sum_{n=1}^{N}\sum_{i=1}^{Z} k_{io} N_i^T N_i q_k. \tag{21}$$

Similarly, the dissipated energy owing to damping is expressed as

$$D_k = -\dot{q}_k^T \sum_{n=1}^{N}\sum_{i=1}^{Z} c_{io} N_i^T N_i \dot{q}_k. \tag{22}$$

2.3. Analysis of the Disturbance Force Input of the Shutter Rotation Shaft-bearing System

Additionally, the sources of disturbances in the shutter system were modeled and analyzed. The blades of the test piece are equivalent to a rigid body, and the fundamental frequency of the test piece blade is considerably higher than the frequency to be measured. Therefore, the mass of the blade was considered equivalent to the test piece, it was then verified by comparison with the test results. The source of the shutter disturbance force is primarily the excitation of the blade rotation and unbalanced mass excitation from defected components during the use of the bearing, as presented in Figure 5.

In Figure 5, the shutter blade is equivalent to an eccentric mass point of the shutter shaft, m_p is the mass, r is the radial eccentricity, and d is the axial eccentricity. During the shutter exposure process, the static and dynamic unbalanced excitations generated by the blade rotation can be expressed as

$$F_r = m_p r\,\dot{\alpha}^2, \tag{23}$$

$$T_r = m_p r d\dot{\alpha}^2. \tag{24}$$

By decomposing the disturbance force in the coordinate system, we can write

$$F_r|_{x_k y_k z_k} = [F_r\cos\theta(t) F_r\sin\theta(t) 0]^T\ , \tag{25}$$

$$T_r|_{x_k y_k z_k} = [T_r\cos\theta(t) T_r\sin\theta(t) 0]^T\ . \tag{26}$$

Bearing produces additional mass imbalance owing to the mutual movement of internal components, and the excitation of the additional mass imbalance is expressed as

$$F_b|_{x_k y_k z_k} = [U_b\Omega^2\cos\Omega(t) U_b\Omega^2\sin\Omega(t) 0]^T\ , \tag{27}$$

where U_b denotes the dynamic mass imbalance, Ω is rotating speed of the retainer, it can be given by

$$\Omega = 0.5(1 + D_{kb}D_{km}^{-1}\cos\alpha_k)\dot{\alpha}. \tag{28}$$

3. Theoretical Analysis

The Runge–Kutta method was applied to solve the kinetic equations and analyze the response of the disturbance output of the shutter. The shutter disturbance was considered as the only disturbance force input, where eight different speeds were considered. The obtained results were converted to the frequency domain and plotted as a waterfall diagram, which is an appropriate approach to identify the effect of frequency and rotational speed on the disturbances in a rotating system.

Figures 6–10 show the waterfall plots of the forces and moments. The disturbance forces and disturbance moments exhibit relatively large amplitudes at the rotation and multiplication frequencies. The frequencies of these disturbances linearly depend on the speed, disturbances slide along the frequency axis with an increasing speed. The two diagonal ridges of disturbances with the largest amplitude are at the rotation and multiplication frequencies of the red and black dashed lines. According to the response spectra in Figures 6–8,

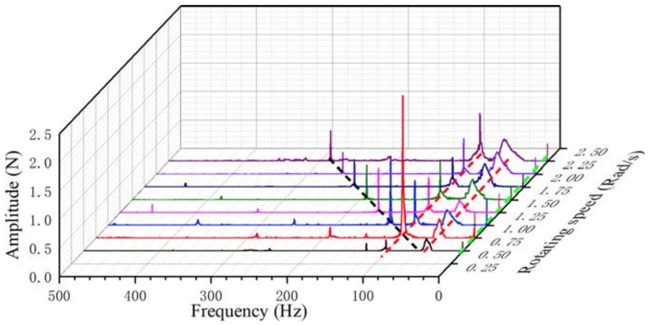

Figure 7. Simulation results of disturbance forces in *Y*-direction.

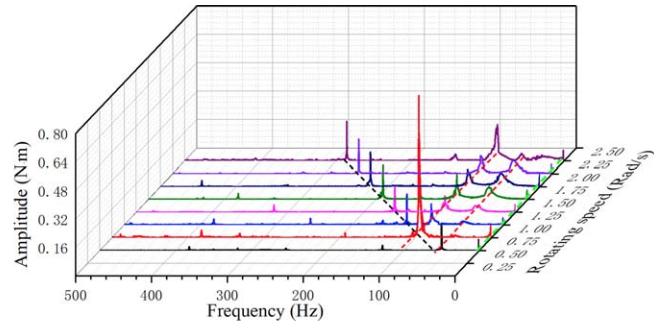

Figure 10. Simulation results of disturbance moments about *Z*-direction.

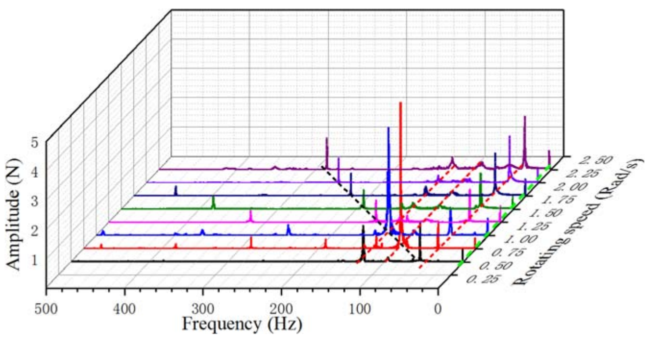

Figure 8. Simulation results of disturbance forces in *Z*-direction.

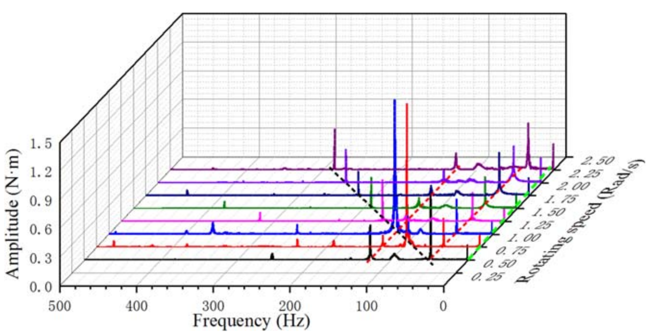

Figure 9. Simulation results of disturbance moments about *Y*-direction.

the disturbance output is dominantly in the radial directions, and at the rotating frequency, no obvious disturbance output in the axial direction appears. Thus, the disturbance output at the rotation frequency is primarily caused by the rotational excitation of the shutter. At high multiplication frequencies, the disturbance induced by the nonlinear vibration of the bearing is considerably richer. The multiple-frequency of the black line, caused by the bearing defects, is the largest of these disturbance ridges, which is clearly visible in the radial and axial directions. Moreover, the radial and axial motions of a bearing system are coupled in theoretical modeling. Therefore, when the bearing system causes a disturbance in the shutter axis, it is bound to cause a similar disturbance in the radial direction. Thus, Figures 6–10 show that at high multiplication frequencies, radial and axial directions have the same spectral characteristics and both appear to be amplified by the structural modes, however, their amplitudes are slightly different, particularly at the structural modes of 98 and 120 Hz.

In summary, the radial disturbance in the shutter is primarily caused by the unbalanced excitation of the blade, whereas the axial disturbance is caused by the nonlinear vibration of the bearing and appears as a high-frequency disturbance in the form of multiplication frequencies. Therefore, it is crucial to consider the nonlinear vibration of the bearing when the disturbance of microvibrations caused by the shutter is analyzed.

4. Experimental

4.1. Experimental Setup

The experimental setup for testing the microvibration force of the shutter is depicted in Figure 11. The setup includes a custom microvibration six-component force plate (Kistler), which is appropriate for measuring the high-frequency response and microvibration forces. The force plate comprises four sets of three-component force transducers containing three pairs of quartz plates, which are mounted between the top and bottom plates through a high preload. It is used for measuring the three components of the force (F_x,F_y,F_z) and moment (M_x,M_y,M_z) in three directions. The force measurement range of the force plate is ±500 N, the force resolution is 0.01 N, the moment resolution is 0.001 Nm, and the natural frequency is 1.8 kHz. The shutter is mounted on the test platform along with the Kistler force plate to vibration interference from the environment. Subsequently, the shutter operates at different speeds and the measured force transducer at each speed is recorded using a data acquisition device. The drive speed curve of shutter are shown in Figure 12.

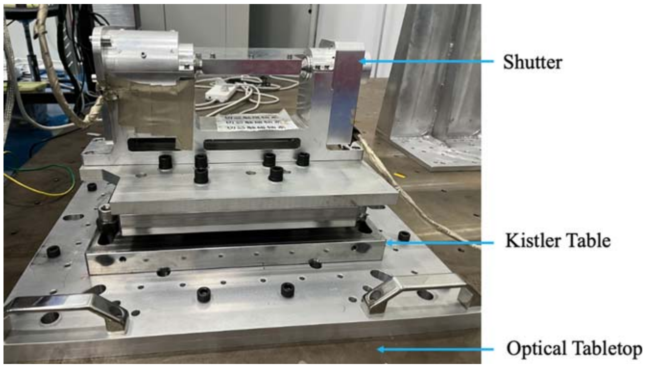

Figure 11. Experimental setup.

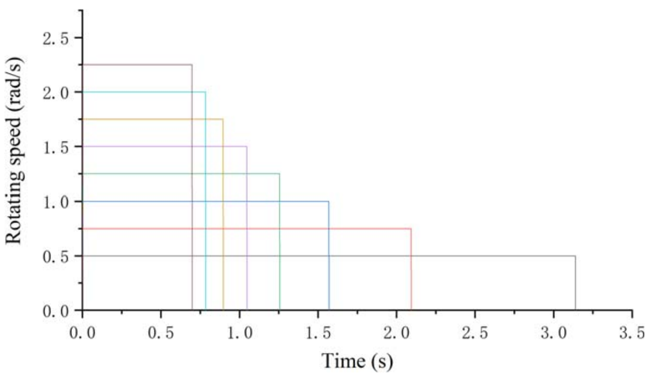

Figure 12. Drive speed curve of shutter.

4.2. Background Noise

After mounting the shutter, the microvibration force and moment tests were performed using the microvibration test platform under the condition that the shutter was at rest and not in operation to obtain the extent of the environmental effect. The test results in Figure 13 show that the maximum force is 0.003 N at a frequency range of 0–500 Hz, and the maximum moment is 0.002 Nm. Therefore, the effect of environmental noise on the experimental results can be ignored.

4.3. Analysis of the Experimental Results

The response curves of disturbance in time domain are shown in Figure 14. The measured signals in the time domain were converted to frequency-domain signals. As shown in Figures 15–19, a three-dimensional waterfall plot is used to represent the amplitude of the disturbance in different frequency bands as a function of the shutter rotation speed.

Figures 15–19 demonstrate that the spectral characteristics of the disturbance in all three directions are identical. Comparing the disturbance amplitudes reveals that the radial disturbance of the shutter is larger than the axial disturbance. According to the response spectra, the disturbance frequency in the low-frequency range corresponds to the unbalanced excitation frequency of the rotation shaft and the amplitude at this frequency is considerably obvious compared to that at high multiplication frequencies. In the high-frequency range, multiplication-frequency disturbances caused by the unbalanced excitation appear, which are primarily caused by nonlinear factors within the system. The largest amplitude appears at the multiplication frequency of the black dotted line. In particular, the nonlinear factors that cause high multiplication-frequency disturbances dominantly stem from the bearing rather than the rotation shaft, primarily owing to factors such as the gap, nonlinear stiffness, friction, and geometric nonlinearity. The radial and axial motions of the bearing system are coupled, and the multiplication-frequency disturbances in both directions have the same spectral characteristics. The red dashed line in the figure shows that the amplitude at the intersection of the multiplication and natural frequencies of the system is significant, which is caused by a dynamic amplification phenomenon generated by the structural mode excited by the multiplication frequency. These disturbance amplifications caused by structural modes form ridges, which are parallel to the axis, are independent of the shutter speed. This is the most dominant source of disturbance in the microvibrations caused by the shutter component, and the vibration amplitude at the natural frequency is greater than that at the rotational frequency and its multiplication frequency.

This study focused on a steady velocity, the acceleration after 0.01 s, and the deceleration time required to stop. Figure 14 captures the moment that the shutter starts at a speed greater than 1.25 rad s^{-1}. There will be a significant impact force in the z direction, which will gradually stabilize along with the movement of the shutter. At the same speed condition, an impact increase can be found in the y direction before the shutter stops, but it is not particularly prominent compared to the amplitude of the entire running process. Therefore, there are mainly instantaneous force increases in the z and y directions during the shutter startup, and shutter stop, respectively. Moreover, the amplitude does not increase much more compared to the stable movement of the shutter.

5. Discussion

The comparison of the experimental and simulation results proves that the disturbance amplitude at the natural frequency is greater than that at the rotational frequency and its multiplication frequency. The maximum amplitude of the disturbance force is located at the intersection of the natural frequency and disturbance multiplication frequency. In addition, the excitation of the multiplication frequency at the natural frequency is the primary cause of the disturbance. Therefore, the intersection of the rotational and multiplication frequencies with the natural frequency in the design of the shutter speed should be avoided. Moreover, the obtained results demonstrate

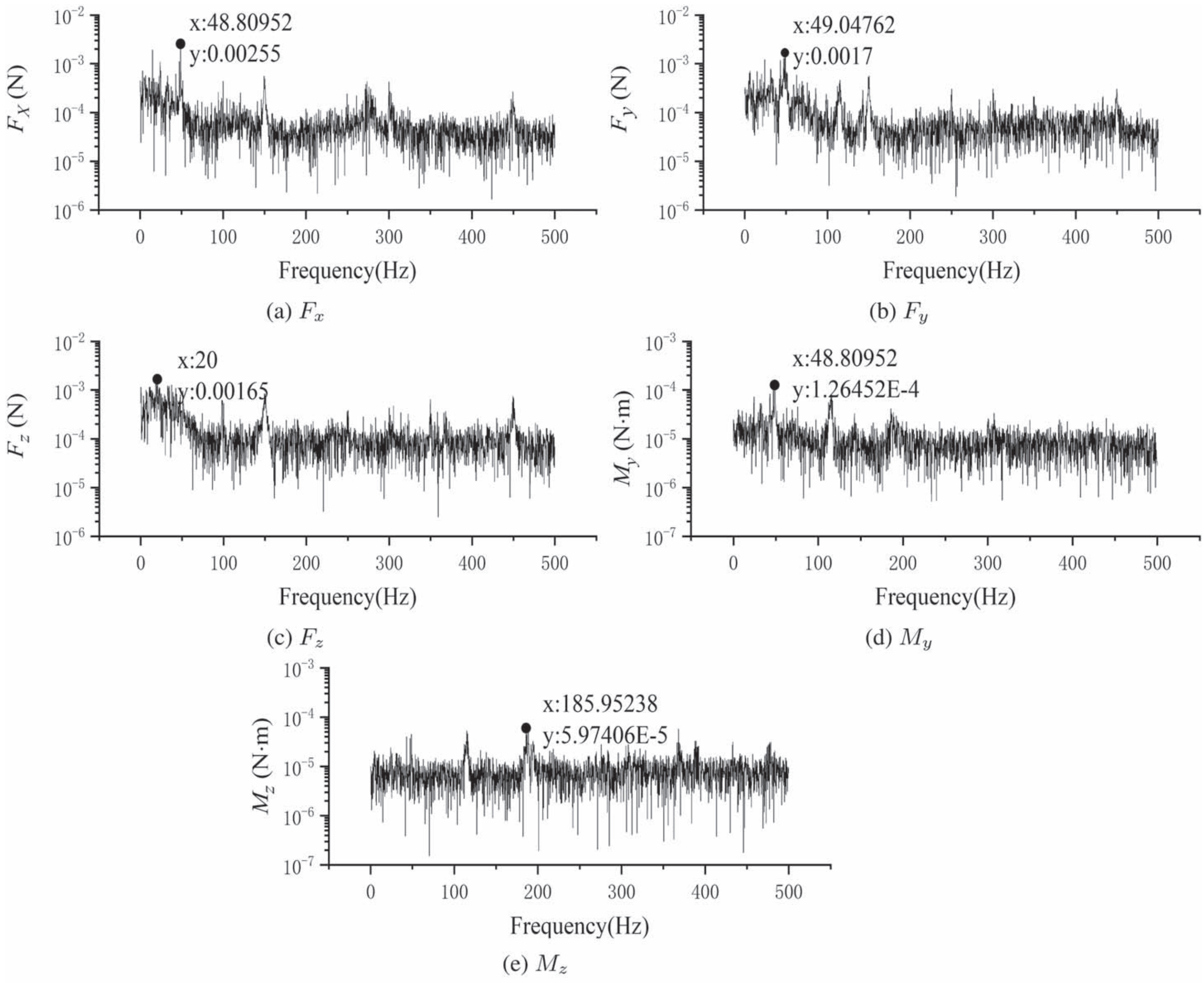

Figure 13. Background noise.

that the disturbance in the *x*-direction includes higher order multiplication frequencies caused by the nonlinear vibration of the bearing. The disturbances in the *y*- and *z*-direction include the rotational excitation of the shutter and higher-order multiplication frequency coupling caused by the nonlinear vibration of the bearing. Figures 6 and 9 demonstrate that certain errors between the theoretical and experimental natural frequencies in the *y*-direction appear. The deviation of the natural frequency might be attributed to the adapter tooling and boundary conditions in the test, which could have some influence on the natural frequency of the system. In addition, changes in the rotating position of the blade have a certain effect on the natural frequency.

As the operating speed of the shutter is approximately 0.75 rad s^{-1}, Figures 20–24 presents a comparison of the theoretical and experimental results of the disturbances generated at a rotating speed of 0.75 rad s^{-1}. The experimental and theoretical frequency values agree satisfactorily. The measure amplitude exhibits unique disturbance spikes at high frequencies, which are owing to defects in the bearing, nonlinearities caused by nonuniform mass, friction, lubrication, etc. Furthermore, nonlinearities generate spikes at the higher order multiplication frequencies during the vibration. Moreover, the magnetic variation during motor operation causes low-amplitude disturbance spikes at higher frequencies. In Figure 14, the response in time domain also has the response of other

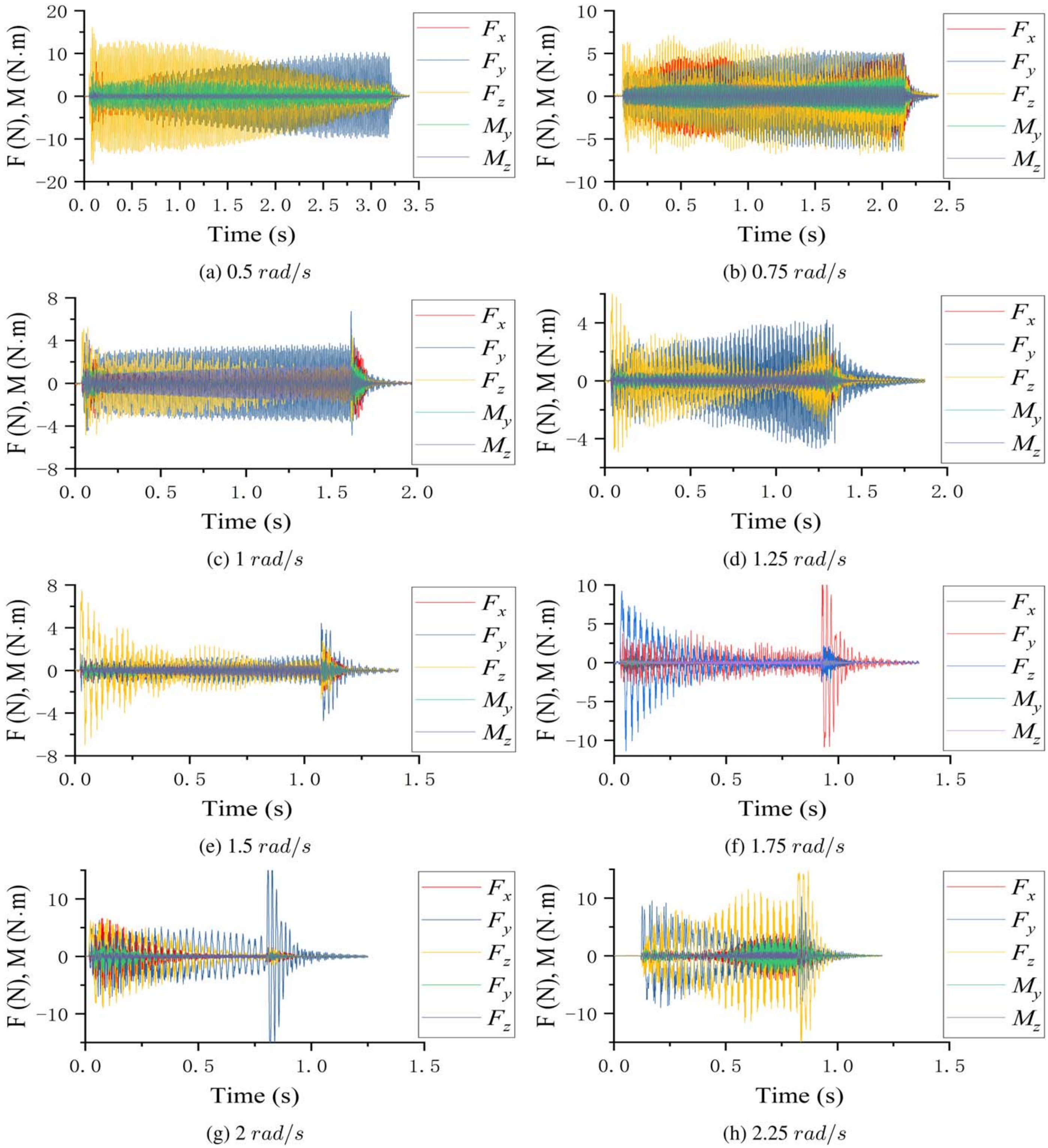

(a) 0.5 rad/s (b) 0.75 rad/s

(c) 1 rad/s (d) 1.25 rad/s

(e) 1.5 rad/s (f) 1.75 rad/s

(g) 2 rad/s (h) 2.25 rad/s

Figure 14. The response curves of shutter disturbance in time domain.

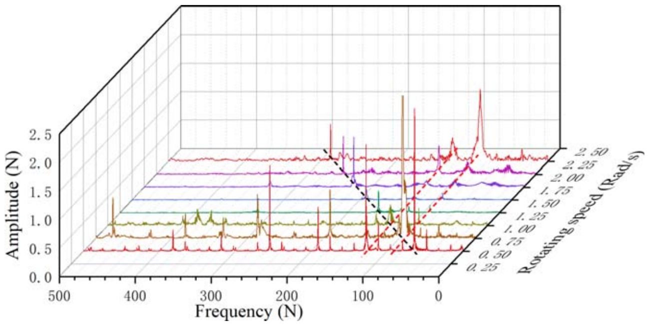

Figure 15. Disturbance forces in *X*-direction.

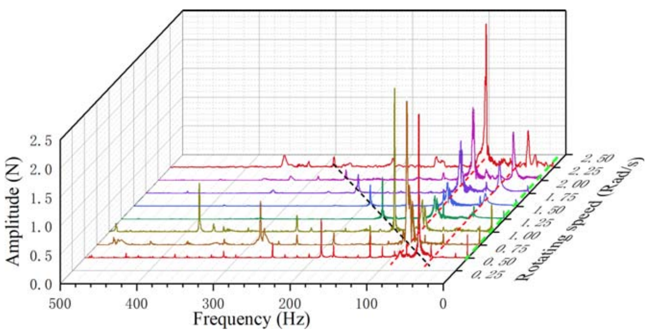

Figure 16. Disturbance forces in *Y*-direction.

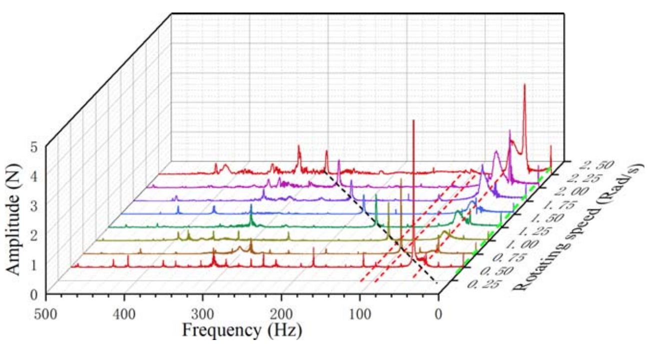

Figure 17. Disturbance forces in *Z*-direction.

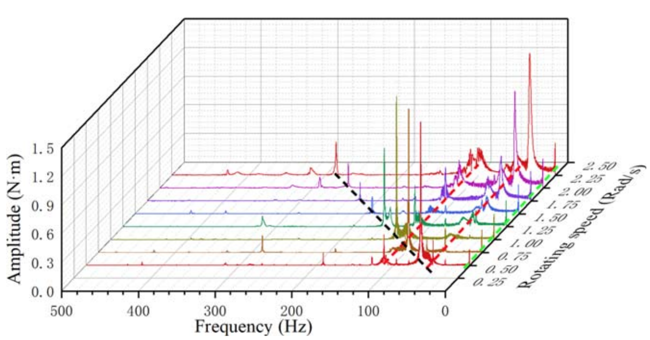

Figure 18. Disturbance moments about *Y*-direction.

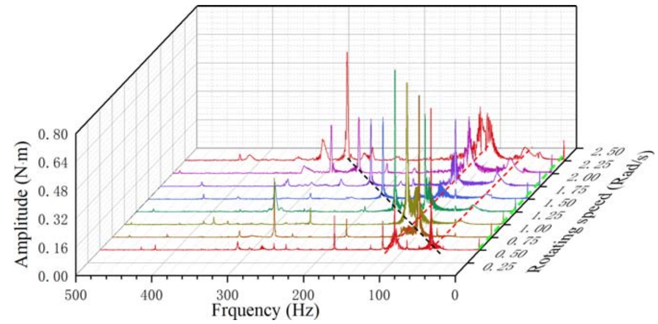

Figure 19. Disturbance moments about *Z*-direction.

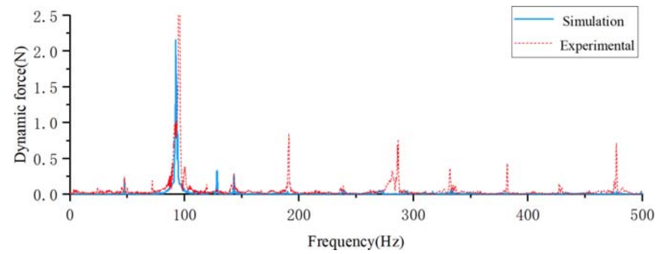

Figure 20. Comparison between experimental and simulation dynamic forces in *X*-direction at a rotating speed of 0.75 rad s^{-1}.

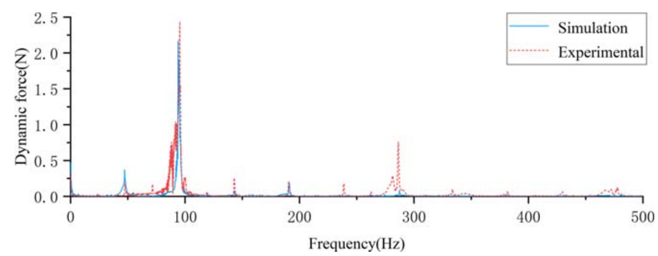

Figure 21. Comparison between experimental and simulation dynamic forces in *Y*-direction at a rotating speed of 0.75 rad s^{-1}.

excitation frequency. These excitation mainly generated by the drive-control modes and driving frequency of motor. The experimental results include various practical disturbance sources, whereas the simulation results are limited to the considered disturbance sources. Thus, some of the disturbance sources in the experimental results are not acquired in the simulation results, which contributes to the difference between the theoretical and experimental amplitudes. In addition, the inevitable interference between microvibrations amplifies or reduces the amplitude. These differences do not affect the accuracy of the theoretical model in predicting the microvibrations of the shutter component.

Future studies on shutter microvibration could explore controlling the vibration generated from the shutter mechanism according to the results of the dynamic model calculation.

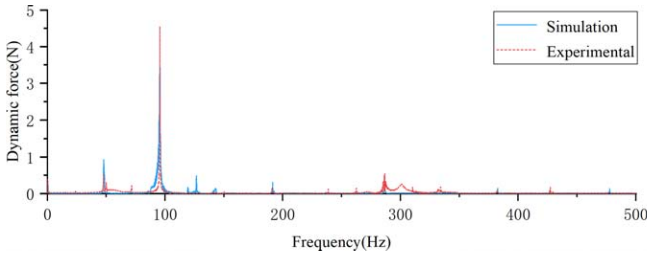

Figure 22. Comparison between experimental and simulation dynamic forces in Z-direction at a rotating speed of 0.75 rad s^{-1}.

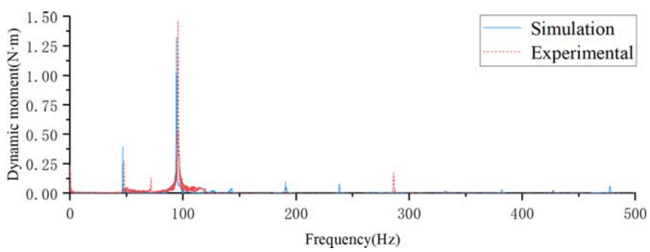

Figure 23. Comparison between experimental and simulation dynamic moments about Y-direction at a rotating speed of 0.75 rad s^{-1}.

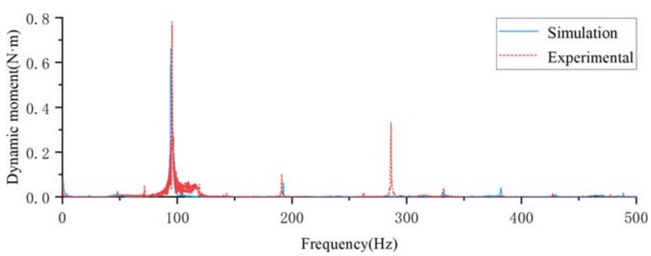

Figure 24. Comparison between experimental and simulation dynamic moments about Z-direction at a rotating speed of 0.75 rad s^{-1}.

Owing to its high reliability, passive control is often used in vibration control of space structures, such as the HST and JWST. The Euclid-VIS in the Euclid Space Mission uses the same type of shutter as the survey camera and has achieved good results with regard to vibration suppression. Passive vibration isolation measures are difficult to apply to the shutter of the survey camera owing to space and mass constraints, and traditional vibration isolation measures weaken the support stiffness of the shutter owing to the low operating frequency of the shutter. Therefore, active magnetic bearings can be used instead of conventional ones to actively control imbalance-induced vibration by actively adjusting the magnetic bearing force. Meanwhile, viable approaches to suppress vibration include optimizing the shutter drive curve, optimizing the transfer path to sensitive components, and installing vibration isolators in front of sensitive components. These methods reduce the vibration effect on the focal plane component induced by the shutter.

6. Conclusion

In this study, a five-degree-of-freedom dynamic model was proposed to analyze the microvibrations of the shutter component. Unlike the three-degree-of-freedom or empirical models, the proposed dynamic model relies on the physical parameters of the shutter. Moreover, the presented model considers the flexibility of the blade and disturbance sources of the microvibrations to guarantee a reasonable accuracy. The proposed dynamic model of the shutter was experimentally verified, thus the results proved that the introduced model could simulate the forces of microvibrations in three directions along with the rocking moments in the x and y axes. The simulation and experimental results reasonably agreed, confirming the effectiveness of the proposed dynamic model in characterizing the disturbances stemmed from different sources. The application of the model can reduce the manufacturing costs and development cycle of the shutter. Furthermore, the proposed model can be used to pre-calculate the values of the generated microvibrations during the design stage to confirm that the microvibrations are within the required range. Otherwise, the parameters can be easily modified in the model before the shutter is actually produced. In addition, components such as bearings can be adjusted to reduce the level of microvibrations until the requirements are fulfilled. Consequently, the proposed dynamics model can accurately simulate microvibrations, reduce the shutter development cycle, and provide a theoretical basis for the development and accurate observation of CSST.

Acknowledgments

We thank the referee for all the helpful suggestions and comments. We are grateful to Prof. Wei Liang for his support and help in the experiment. We acknowledge financial support for the CSST Survey Camera from the China Manned Space Program through its Space Application System.

ORCID iDs

Hu Zhan https://orcid.org/0000-0003-1718-6481

References

Alkomy, H., & Shan, J. J. 2021, JSV, 492, 115
Davis, L. P., Wilson, J. F., & Jewell, R. 1986, NASA Report, 87, 669
Gao, M., Zhao, G. H., Gu, Y. D., et al. 2015, BCAS, 30, 721
Hasha, M. D. 1986, Space Telescope Program Engineering Memo SSS, 218, 175
Hernot, X., Sartor, M., & Guillot, J. 2000, JMD, 122, 83
Li, L., Tan, L. Y., Kong, L., et al. 2018, MSSP, 100, 360

Liang, W. 2021, Research on Micro-vibration Modeling and Suppression Technology of the Survey Camera, Doctoral Dissertation, Univ. Electronic Science and Technology of China
Liu, C. C., Jing, X. J., Daley, S., et al. 2015, MSSP, 56, 55
Liu, J., Ke Tang, C., & Min Shao, Y. 2019, MMT, 135, 27
Liu, K. C., Maghami, P., & Blaurock, C. 2008, in AIAA Guidance, Navigation and Control Conf. and Exhibit (Honolulu, Hawaii: AIAA), 18
Luo, Q., Li, D. X., Zhou, W. Y., et al. 2013, JSV, 332, 4496
Masterson, R. A., Miller, D. W., & Grogan, R. L. 2002, JSV, 249, 575
Meza, L., Frank, T., Anandakrishnan, S., et al. 2005, in 27th Annual AAS Guidance and Control Conf. (San Diego, CA: AAS)
Su, D. Q., & Cui, X. Q. 2014, RAA, 14, 1055
Tang, L., Zhang, K. B., Guan, X., et al. 2020, ASR, 65, 271
Wang, H., Han, Q. K., Luo, R. Z., et al. 2017, JSV, 406, 124
Xia, M. Y., Qin, C., Wang, X. M., et al. 2021, MSSP, 146, 107007
Zhan, H. 2011, SSPMA, 41, 1441
Zhan, H. 2021, CSB, 66, 1290
Zhou, W. Y., LI, D. X., Luo, Q., et al. 2012, CJA, 25, 640